optica

Swept source optical coherence tomography and tunable lens technology for comprehensive imaging and biometry of the whole eye

Ireneusz Grulkowski,[1,*] Silvestre Manzanera,[2] Lukasz Cwiklinski,[1] Franciszek Sobczuk,[1] Karol Karnowski,[1,3] and Pablo Artal[2,4]

[1]Institute of Physics, Faculty of Physics, Astronomy and Informatics, Nicolaus Copernicus University, ul. Grudziadzka 5, 87-100 Torun, Poland
[2]Laboratorio de Óptica, Instituto Universitario de Investigación en Óptica y Nanofísica, Universidad de Murcia, Campus de Espinardo, E-30100 Murcia, Spain
[3]Current address: Optical+Biomedical Engineering Laboratory, School of Electrical, Electronic and Computer Engineering, University of Western Australia, 35 Stirling Hwy., Crawley 6009, Australia
[4]e-mail: pablo@um.es
*Corresponding author: igrulkowski@fizyka.umk.pl

Standard optical systems in ophthalmology are strictly dedicated either to retinal or to anterior segment imaging due to the refractive properties of the eye. We demonstrate a swept source optical coherence tomography platform with an electrically tunable lens (ETL) for versatile 3D *in vivo* imaging of both the eye's anterior segment and the retina. The optimized optical setup with adaptive operational states of the ETL permits focusing on the retina and on the anterior segment. Dynamic control of the optical beam focus allows for OCT image enhancement, leading to the visualization of the vitreous details at both the vitreo-lenticular and vitreo-retinal attachment sites in an unprecedented manner. ETL tuning enables sequential visualization of the anterior and posterior segment of the eye, and such whole eye imaging can be also used to perform quantitative ocular biometry.   © 2018 Optical Society of America

1. INTRODUCTION

The ocular structures constituting the optical system of the eye produce images on the retina that initiate the visual process [1]. Examination of the eye is a common clinical procedure in the diagnosis and therapeutic management of both eyes' anterior segment and retinal disorders. In particular, visualization of the whole eye morphology and the orbit makes it possible to evaluate clinically relevant features in diseases like ocular tumors [2]. Current modalities for eye globe imaging include ultrasound, magnetic resonance imaging, and computer *x*-ray tomography [3–5]. Those techniques, however, are either relatively expensive or invasive or require contact with the eye, or the image resolution is too low to visualize subtle details. Therefore, an optical platform enabling comprehensive visualization of the entire eye could significantly expand both research and clinical ophthalmic capabilities.

Optical coherence tomography (OCT) has revolutionized ophthalmic diagnostics due to its noninvasiveness and ability to generate cross-sectional and volumetric images of micrometer resolution. Initially, OCT instruments were designed for imaging either the anterior or posterior eye zones. Using OCT systems to image the whole eye presents several challenges. The first

challenge is associated with the limited imaging depth. Clinical OCT instruments are usually characterized by depth ranges up to 2–3 mm to be able to visualize retinal and choroidal tissues. However, imaging of the anterior chamber requires a depth range of 5 mm [6]. Full-range techniques were later applied in Fourier-domain/spectral-domain OCT (SD-OCT) technology to obtain images of the entire anterior segment of the eye including the crystalline lens [7]. The first reports on whole eye imaging were implemented in SD-OCT with quasi-simultaneous imaging at multiple depth ranges. This was realized practically through integration of two OCT systems [8–10], with an optical/mechanical switch in the reference arm [11,12] or in the detection arm of the interferometer [13,14]. However, recent developments in Fourier-domain/swept-source OCT (SS-OCT) technology, as well as advances in rapidly tunable light sources, enabled depth ranges exceeding tens of millimeters to be achieved without any complex hardware or software modifications [15–17]. The availability of long imaging ranges stimulated applications of OCT systems in ocular biometry [18], some of which are already commercially available [19–25].

Second, the eye's optics prevents the focusing of light on the retina and the anterior segment simultaneously without

sacrificing lateral resolution. Some commercial OCT instruments are dedicated to retinal imaging with an optional anterior segment imaging mode. In this case, adding or removing an adapter lens in the object arm of the system is required for switching between the imaging modes [6]. Laboratory systems for whole eye imaging have used a sample arm with a dual-focus configuration in the same or two separate spectral bands as well as polarization-encoded paths in the interface for retinal and anterior segment imaging [8,9,13,16]. Moreover, full-eye-length SS-OCT imaging with a large-depth-of-focus optical beam was presented [15].

Finally, since OCT uses light with a wide spectrum, chromatic dispersion must be considered. The dispersion mismatch is usually compensated either hardware-wise in the system by inserting glass of the appropriate thickness or software-wise by multiplication of the signal and an exponential function (second- and third-order terms) in the postprocessing. Light propagating inside the eye is more dispersed when it reaches the retina. Therefore, once dispersion-matched images are obtained for the anterior segment, additional compensation is required to obtain good quality retina images.

Miniaturization of optical systems required the development of new technologies, including tunable lenses that change their optical power in proportion to an applied voltage. Due to advances in microsystem engineering, different tuning mechanisms have been proposed including electrowetting, pneumatic pressure, magnetic actuation, electroactive materials, electrostatic actuation, liquid crystals, and acousto-optics [26]. The lenses with a tunable focus are primarily used in zoom objectives and machine vision, and were recently applied in microscopic systems [27–29]. Utilization of electrical or acousto-optic tunable lenses can improve the performance of the OCT setup [30,31]. Electrically tunable lenses (ETLs) found an interesting application in intraoperative OCT for adjusting defocus [32,33]. Moreover, they have also been used in testing and correction devices [34–36].

In this work, we demonstrate an optical instrument with tunable lens technology for versatile visualization of the eye morphology, and particularly for providing unprecedented (to our knowledge) high-quality 3D images of both the anterior and posterior areas of the vitreous. We investigate the performance of the lens and its impact on the SS-OCT system. We present how the focus tuning affects the image quality in both anterior segment and retinal imaging modes. In addition, we show quasi-simultaneous imaging of the retina and anterior segment (whole eye imaging) that can be used for precise optical ocular biometry (measurement of intraocular distances).

2. EXPERIMENTAL SETUP

An ETL (EL-10-30-C, Optotune AG, Switzerland) was incorporated into a long-range SS-OCT system. We first evaluated the performance of the ETL illuminated by the collimated beam [Fig. 1(a)]. The measurements were performed with and without an offset diverging lens ($f = -100$ mm). Beam profiling of light leaving the tunable lens was done automatically with a 2D CMOS camera (uEye, UI-1240SE-M-GL, Imaging Development Systems GmbH, Germany) on a long-range translation stage. The wavefront of the light beam exiting the ETL was measured with a Hartmann–Shack wavefront sensor (HSWS). The ETL exit plane was transformed to the HSWS lenslet array plane with a relay ($4f$) lens system [Fig. 1(a)]. The current of the tunable lens was varied over a range between 0 and 300 mA.
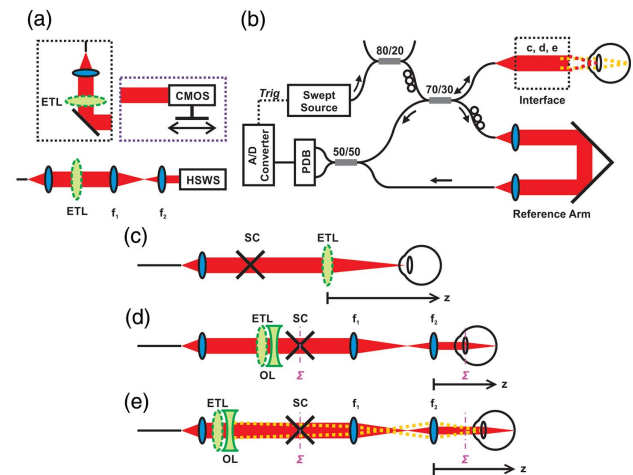
Fig. 1. Experimental setup. (a) Setup for beam profiling and wavefront sensing. CMOS, camera; HSWS, Hartmann–Shack wavefront sensor; ETL, electrically tunable lens; $f_1 = 100$ mm, $f_2 = 50$ mm. (b) SS-OCT system. Configurations of the object arm with tunable lens: (c) anterior segment imaging, (d) retinal imaging, (e) whole eye imaging. PDB, balanced photodetector; SC, galvanometric scanners; OL, offset lens; f_1 and f_2, relay optics lenses ($f_1 = 100$ mm, $f_2 = 50$ mm); Σ, pivot plane.

The long-range SS-OCT system [Fig. 1(b)] utilized a customized wavelength-swept engine operating at a central wavelength of 1050 nm and a sweep rate of 50 kHz (Axsun Technologies Inc., USA). Decreasing the sweeping rate resulted in an enhanced coherence length the source, and therefore improved the depth performance of the system (only ∼6 dB signal drop at a 14 mm depth, measured with a high-sampling-frequency oscilloscope). The light entering the system was split into the sample (interface) and single-pass reference arms. The light coming back from both arms interfered at the 50:50 fiber coupler, and the interference signal was detected by a balanced photodetector (PDB-480-C, Thorlabs Inc., USA). The acquisition system contained a field-programmable gate array module (National Instruments, USA) with a digitizer with a 0.8 GS/s (gigasamples/second) bandwidth. The obtained sensitivity was 103 dB (1.9 mW incident on the object), and the signal roll-off was –6 dB at 11 mm. The laser wavelength tuning range resulted in an axial resolution of 8 μm in air.

Three configurations of the sample arm with the ETL were tested experimentally: anterior segment imaging using the ETL as the objective lens [Fig. 1(c)], retinal imaging with the ETL to tune the focus around the retinal and choroidal layers [Fig. 1(d)], and whole eye imaging based on (quasi-)simultaneous imaging of the anterior segment and the retina [Fig. 1(e)]. The parameters of those configurations are given in Table 1.

In all experiments, we used two different scanning protocols (Fig. 2). The first one included 50 horizontal B-scans (1000 A-scans each) repeated at the same position during slow tuning of the ETL current. The second protocol was a sequential cross consisting of 25 perpendicular (sagittal and horizontal) B-scans (1000 A-scans each). In both cases, the frame acquisition time was 20 ms, and the frequency of the ETL tuning (1 Hz) was set so that the total acquisition time (1 s) was equal to the period of focus tuning.

Table 1. Operational Modes of OCT System with Tunable Lens[a]

Parameter	Anterior Segment Imaging	Retinal Imaging	Whole Eye Imaging
ETL distance from the scanners[b]	+140 mm	−90 mm	−170 mm
ETL waveform and frequency		Sine, 1 Hz	
ETL current range	130–180 mA	50–200 mA	100 mA (ret.) to 300 mA (AS)
Offset lens	NO	YES ($f = -100$ mm)	YES ($f = -100$ mm)
Axial range (air)		22.3 mm	
Axial resolution (air)		8 μm	
Lateral resolution	43 μm	15 μm	15 μm (ret.) 47 μm (AS)

[a]AS, anterior segment; ret., retina.
[b]Positive value means behind the scanners; negative value indicates ETL is positioned in front of the scanners.
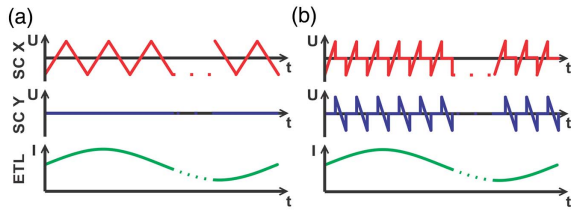
Fig. 2. Scan protocols used in this study. Driving signals are applied to the scanners (SC) and to the tunable lens. (a) Sequential B-scan protocol, (b) sequential cross scan protocol.

We applied the instrument to image the eyes of healthy volunteers. The procedures and protocols were approved by the institutional review boards at the Nicolaus Copernicus University in Toruń and the University of Murcia. The research adhered to the tenets of the Declaration of Helsinki.

3. RESULTS

A. Performance of the Electrically Tunable Lens

To investigate the performance of the tunable lens, it was illuminated with a collimated light beam, and it was driven with different current levels. The light intensity distribution behind the lens was measured with a CMOS camera to reconstruct axial beam profile. The wavefront shape and optical power were measured with the HSWS.

Figure 3(a) shows beam profiles for two selected current values applied to the ETL. The focus can be tuned over a range of 80–200 mm, and we selected the driving current values so that $f = 137$ mm and $f = 80$ mm were obtained. Figure 3(b) demonstrates the reconstructed wavefront exiting the ETL for the current $I = 0$ mA, and Visualization 1 presents the wavefront dynamics for different current values. The optical power of the
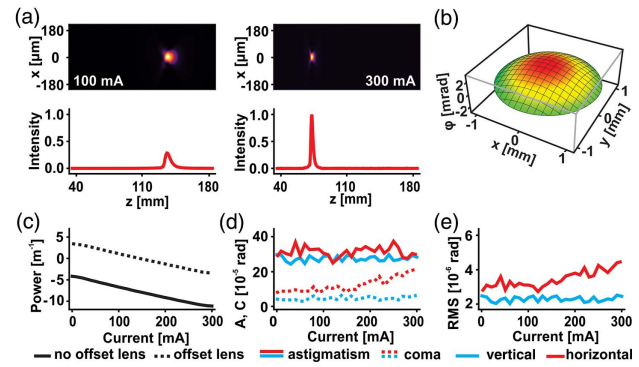
Fig. 3. Operation performance of the electrically tunable lens. (a) Horizontal sections and axial profiles of light intensity behind the ETL for current values $I = 100$ mA and $I = 300$ mA, (b) shape of the wavefront exiting the ETL (Visualization 1), (c) tunable lens power as a function of applied current with and without an offset lens, (d) magnitude of wavefront astigmatism (A) and coma (C) for vertical and horizontal orientations of the ETL without offset lens showing gravitationally induced aberrations, (e) root mean square (RMS) of higher-order aberrations of the wavefront exiting the vertically and horizontally oriented ETL.

imaging system changes linearly with the driving current [Fig. 3(c)]. Compounding the ETL with a particular offset lens enables the available range of focal lengths to be shifted. Additionally, the ETL introduces gravity-induced aberrations [Figs. 3(d) and 3(e)], i.e., magnitude of astigmatism and coma, defined by $A = 2\sqrt{(c_{2,2})^2 + (c_{2,-2})^2}$ and $C = 3\sqrt{(c_{3,1})^2 + (c_{3,-1})^2}$, respectively, where the coefficients $c_{2,2}$, $c_{2,-2}$, $c_{3,1}$, and $c_{3,-1}$ are Zernike coefficients of primary astigmatism and primary coma, as well as higher-order aberrations. The ETL in a system with a vertically oriented optical axis provided less aberrations.

Thereafter, we tested the three optical configurations that have been optimized with respect to their corresponding applications.

The numerical simulations of the beam in free space behind the front lens [cf. Figs. 1(c)–1(e)] in each configuration were based on the beam propagation method in the Fourier optics formalism [37]. The simulation results demonstrate how the axial profile of light intensity changes for the entire tuning range of power of the ETL lens (Fig. 4). Two current levels have been applied to the ETL in each configuration, and the numerical intensity axial profiles were compared with the experimentally measured beam profiles. The anterior segment interface with the ETL as an objective lens enables focus tuning [Fig. 4(a)]. The position of the ETL in the retinal imaging interface was set to provide slight focusing or defocusing of the beam incident on the eye [Fig. 4(b)], which allowed for focus tuning across the retinal layers. The third configuration, with sequential switching between anterior segment and retinal imaging operational modes, requires the light to be focused in the pupil plane or collimated beam, respectively [Fig. 4(c)].

B. Anterior Segment Imaging with Adjustable Focus

The ETL took the place of the objective lens in the anterior segment imaging mode to enable focus tuning. The distance of the lens from the galvanometric scanners corresponded to the mean front focal length of the ETL ($f = 140$ mm). The ETL was driven at a frequency of 1 Hz (Table 1). We acquired repeated
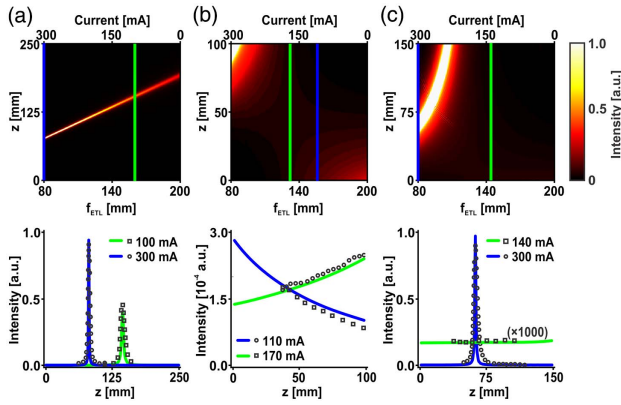
Fig. 4. Numerical simulations and experimental data of axial intensity profiles of the beam for different states of the ETL. Upper panel shows intensity maps along the optical axis for the entire tuning range of the ETL. Lower panel shows calculated intensity profiles for two selected ETL current values in each imaging mode (solid green and blue), along with the profiles measured experimentally (dots). (a) Anterior segment imaging interface, (b) retinal imaging interface, (c) whole eye imaging interface. Optical axis z was defined in Figs. 1(c)–1(e) for each imaging mode.

horizontal B-scans to assess the image quality at different ETL tuning phases. By adjusting the focus, one can shift the depth at which an effective increase in collected photons appears [see selected images in Fig. 5(a) and the movie in Visualization 2]. The lens tuning amplitude was set here to provide the maximum effective axial tuning range. The progressive image quality improvement was demonstrated by the implementation of the focus stacking technique, which finally allowed us to achieve a high signal from the structures located beyond the depth of focus (Visualization 2). Due to the variable back focal length of the tunable objective lens, the interface does not provide telecentric scanning during most of the period of tuning, which results in modulation of the transverse scanning range. However, this undesirable effect can be compensated by proper image resampling.

Depending on the current levels applied to the tunable lens, one can enhance the OCT signal from a desired depth. Such precise control of the focus position can be used in volumetric imaging. Therefore, the imaging of the posterior crystalline lens

and anterior vitreous can be optimized [Fig. 5(b)]. The signal below the lens capsule has been segmented, and the *en face* projections are based on sum voxel [sum voxel projection (SVP)] or maximum intensity [maximum intensity projection (MIP)]. The projection images reveal vitreo-lenticular interface morphology [Fig. 5(b)]. The opacifications visible below the posterior interface of the crystalline lens have a regular shape [color depth coding was applied in Fig. 5(b)], which can be easily distinguished in volumetric imaging (Visualization 3).

C. Retinal Imaging with Adjustable Focus

Unlike anterior segment imaging systems, retinal scanners require illumination of the eye with a collimated optical beam. Accordingly, we inserted the ETL with the offset lens ($f = -100$ mm) into the sample arm for retinal imaging. The ETL was placed 90 mm before the beam hits the galvanometric scanners (Table 1). Hence, tuning of the effective focus at the retinal plane was possible, without significant distortions. The pupil of the eye needed to be positioned in the pivot point of the relay optics. Sequential B-scans of the retina were acquired during ETL tuning (Visualization 4).

Tuning of the focal position, via current applied to the ETL, affects the retinal and choroidal images [Fig. 6(a)]. In particular, effective enhancement of the signal from the vitro-retinal interface is observed when the focus is placed in front of the retina. Furthermore, by shifting the focus deeper, different layers of the retina structure can be enhanced. Finally, the choroid demonstrates a higher signal when the focus coincides with deeper retina layers. A set of sequential B-scans, acquired for different focus positions, is used to generate focus stacked cross sections with enhanced quality and a superior visualization of the posterior vitreous compared to a single B-scan from the set [Fig. 6(a) right and Visualization 4]. Modulation of the defocus over the entire cycle of the ETL tuning supplemented with focus stacking leads effectively to an unprecedented image of the retina, with enhanced visualization of the microstructural features of the transparent medium such as the posterior vitreous.

The ETL current level corresponding to the best visualization of the vitreous was used to acquire an additional 3D data set [Fig. 6(b) and Visualization 5]. Segmentation of the vitreo-retinal interface allowed us to generate fundus projections showing the distribution of opacities in the posterior vitreous via color coding
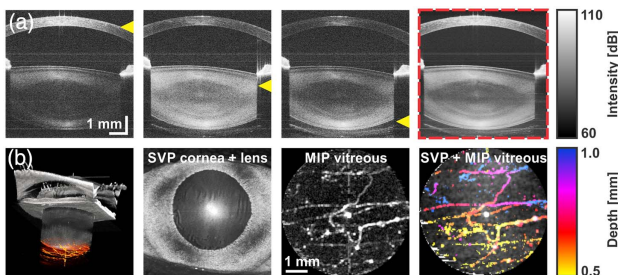
Fig. 5. SS-OCT imaging of the anterior segment with tunable focus. (a) Anterior segment OCT images for different ETL current values (focus position indicated by a yellow triangle) and a composite image generated by focus stacking of 50 cross sections (with red dashed outline). The change in image quality is demonstrated in Visualization 2. (b) Enhanced 3D visualization of anterior vitreous opacifications (Visualization 3): rendering of volumetric data set, *en face* image, MIP, and combined SVP and MIP with depth encoding.
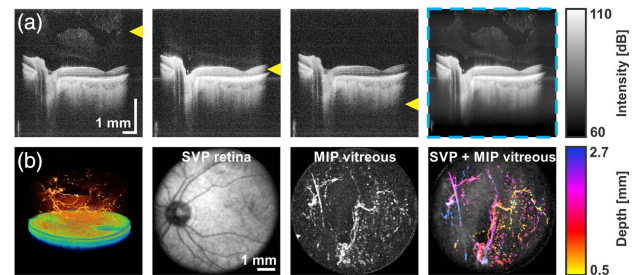
Fig. 6. SS-OCT imaging of the retina with tunable focus. (a) Retinal OCT images for different ETL current values (focus position indicated by a yellow triangle) and a composite image generated by focus stacking of 50 cross sections (with blue dashed outline). The change in image quality is demonstrated in Visualization 4. (b) Enhanced 3D visualization of posterior vitreous opacifications (Visualization 5): rendering of volumetric data set, retinal fundus image, vitreous MIP, and combined SVP and MIP with depth encoding.

of a maximum intensity projection map. A 3D rendering of the volumetric data set provided an insight into the morphology of the vitreous from different perspectives (Visualization 5).
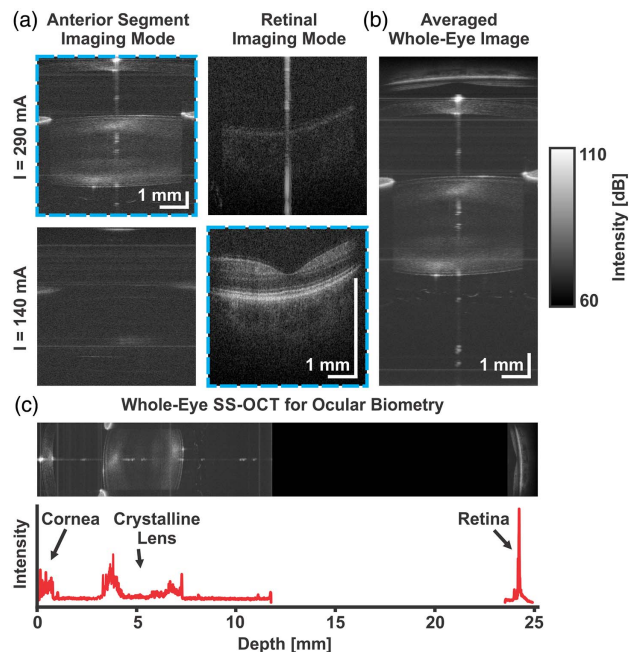
D. Quasi-Simultaneous Imaging of the Whole Eye

The last operational mode of the instrument with a tunable lens enabled fast switching between anterior segment and retinal imaging modes. In this case, the setup for retinal imaging was used but the ETL with the offset lens was moved back to provide greater beam divergence (Table 1). Therefore, it was possible to obtain a collimated (low ETL current) or focused (high ETL current) beam at the pupil plane. The ETL current was switched between B-scans and anterior segment and retina images were acquired alternately.

Figure 7(a) shows the images of the anterior segment and the retina for two states of the ETL (dashed outline), and Visualization 6 shows how the switching between operational modes can be achieved with the ETL tuning. The data set was processed twice to account for dispersion mismatch by the ocular media. The averaged cross section of the eye is presented in Fig. 7(b). The signal from the retina appears as a complex conjugate, but does not coincide with the signal from the anterior segment. The lateral scan range was estimated with an artificial eye. The axial profile of the light intensity scattered/reflected from the ocular structures could be extracted from the image [Fig. 7(c)] and used to calculate intraocular distances, including axial eye length.

E. Optical Biometry

To fully demonstrate the potential of our system in optical biometry applications, we imaged a group of seven healthy subjects using two devices: our long-range SS-OCT system and the

Fig. 7. Quasi-simultaneous OCT imaging of the whole eye. (a) Switching between imaging modes with the ETL (Visualization 6), (b) composite image of the whole eye, (c) composite image of the whole eye after unfolding, with corresponding axial profile of light intensity showing reflections from the ocular components.
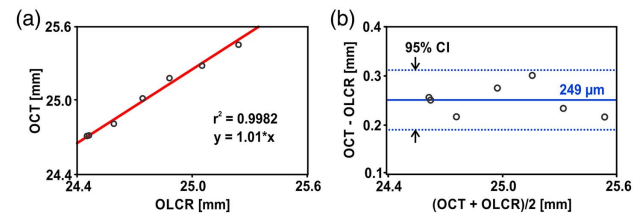
Fig. 8. Ocular biometry based on tunable lens SS-OCT. (a) Correlation plot of axial eye length (AL) between SS-OCT and OLCR (Lenstar), (b) Bland–Altman plot showing agreement between the methods. The solid horizontal line indicates bias, and the dashed lines show 95% confidence interval (CI).

commercial biometer based on optical low-coherence reflectometry (OLCR; Lenstar, Haag-Streit AG, Switzerland). Each subject was measured five times by the same operator. It is crucial in ocular biometry to perform measurements along the visual axis of the eye. Therefore, with the assistance of two perpendicular B-scans in a live preview, the subject's eyes were aligned with respect to the scanning head by simultaneous centering of the pupil and fovea.

The corneal, lenticular, and retinal reflections were identified in the axial profile [Fig. 7(c)], and this enabled calculation of all intraocular distances: central corneal thickness (CCT), aqueous depth (AD), anterior chamber depth (ACD), lens thickness (LT), vitreous depth (VD), and axial eye length (AL). The refractive indices for optical path length correction were estimated based on a previous study [18]. Correlations between the instruments were assessed using Pearson correlation coefficients, and the agreement between the methods was assessed with Bland–Altman analysis. Both the bias and 95% confidence interval were calculated. We used a paired t-test to analyze statistical significance.

A clinically relevant example of biometric measurement is to provide the AL of the eye. The AL measurements with SS-OCT are well correlated ($r = 0.9999$) with the OLCR biometer [Fig. 8(a)]; however, a statistically significant bias (249 μm) is observed in the Bland–Altman plot [Fig. 8(b)]. An overview of the assessment of the prototype SS-OCT biometer and commercial OLCR biometer is given in Table 2. The SS-OCT technique with tunable focus provides highly reproducible measurements of the AL with an accuracy of 18 μm, which is comparable to other optical biometers.

Table 2. Statistical Analysis of Intraocular Distances Measured with SS-OCT and Dynamic Focusing

Parameter	Pearson Correlation Coefficient	Intraclass Correlation Coefficient	Intersession Standard Deviation [μm]
CCT	0.9738	0.9618	9
AD	0.9867	0.9947	39
ACD	0.9812	0.9947	39
LT	0.9095	0.9778	47
VD	0.9565	0.9976	24
AL	0.9940	0.9985	18

4. DISCUSSION AND CONCLUSIONS

The tunable lens is an active optical element that enables flexible choice of its refractive power and focal length. The range of optical power tuning can be further extended by adding a proper offset lens. We investigated the performance of the ETL using beam profiling and wavefront sensing. The maximum frequency accepted by the lens was determined by its settle time, which in the current model was 2.6 ms. That is the reason why switching between the imaging modes was synchronized with B-scan, rather than A-scan, acquisition. High-speed focus tuning at the frequency of the swept source rate would facilitate switching of the operational modes on an A-scan basis. However, this would require different tunable lens technology. On the other hand, the disadvantages of the ETL included its thermal instability, small aperture, and higher-order aberrations. Those limitations, however, will likely be removed with further development of the tunable lens technology.

Gravity-related aberrations introduced by the ETL are relevant in high numerical aperture (NA) microscopic systems. However, the optical configurations designed in the present study are characterized by a relatively low NA. Moreover, the aberrations (i.e., coma and astigmatism) of the object (eye) are a few orders of magnitude higher than the ETL-induced aberrations [38,39]. Therefore, we did not observe significant differences in OCT image quality when the ETL was oriented horizontally versus vertically.

The integration of adaptive lens technology with SS-OCT provided a powerful tool for studying the impact of dynamic focus on OCT image quality. In this work, we identified and implemented three imaging modes: anterior segment imaging, retinal imaging, and a combination of the two yielding whole eye imaging that is a quasi-simultaneous imaging of the anterior segment and the retina. Although the depth range of our SS-OCT system is 22 mm in air, which is rougly 2 × shorter than what is required for imaging through the eye length, the demonstrated whole eye imaging takes advantage of the thickness of the vitreous, which separates the signal from the anterior segment and the retina. We set the position of the reference mirror in such a way that the anterior segment and retinal structures did not superpose each other in the OCT image. Therefore, no complex resolved technique was necessary here.

The central wavelength of 1 μm used in the setup should be considered as the most optimized spectral region for anterior segment and retinal imaging from all available bandwidths. Although a system at 800 nm would provide higher axial resolution with the same bandwidth of the source, the availability of high-speed wavelength-tunable light sources in this range is very limited. Equally important, scattering at longer wavelengths is lower, which assures deeper penetration into tissue. We have chosen swept source technology that offers the highest detection sensitivity among all generations of OCT technologies. Moreover, with modern swept source laser technology, SS-OCT does not suffer significantly from a signal drop with depth, which was advantageous for our long-range imaging.

Focus tuning during OCT image acquisition allows for enhancement of image quality. The proposed approach employing focus tuning also facilitates imaging of relatively deep objects with preservation of lateral resolution over the entire probed volume. Therefore, it was possible to obtain retinal and anterior segment SS-OCT images with high sensitivity, so that the details of the vitreous can also be imaged. Through implementation of focus-tunable optics, we gained a better insight into the microstructure of opacifications in both vitreo-lenticular and vitreo-retinal attachment sites (Visualization 2, Visualization 3, Visualization 4, Visualization 5, and Visualization 6). Application of tunable focus is another method for effective vitreous imaging, which might be helpful in monitoring vitreous surgery. The current study is limited to the visualization of the vitreous near the crystalline lens and the retina in two separate imaging modes that need readjustment. However, further developments should enable imaging of the vitreous through its entire depth. Although vitreous interfaces are the areas of the eye that have been outside the normal range of OCT systems, these zones may have clinically relevant importance if imaged properly. In addition, the approach presented can be advantageous for automatic refractive error compensation for retinal imaging with no mechanical action. Consequently, it facilitates easy adjustment of optics during the retinal scanning procedure.

Focus tunability of the lens allows both the anterior segment and retinal imaging modes to be performed in a single scanning procedure where the focus can be consecutively tuned between the cornea, the crystalline lens, and the retina without any hardware modification of the optical setup. This whole eye imaging mode provides visualization of ocular components, and requires image distortion correction due to fan scanning and refraction of the light. The anterior segment image appears slightly angled, because the optical axis of the system was aligned with the volunteer's visual axis, and thus was offset from the optical axis of the eye by a few degrees.

The whole eye imaging mode can be used for eyes with any axial eye length. If the depth range of the OCT system enables imaging of the full eye length, no mirror image is observed. However, a limited depth range of the SS-OCT system used in the current study forced us to take advantage of the retinal mirror image, which caused partial loss of the information on the vitreous along the full visual axis. The depth range can be doubled through the implementation of the full-range technique. The proposed configuration allowed us to avoid superposition of the anterior segment and the retinal signals from both conjugated Fourier half-spaces via a proper adjustment of the reference arm length. If the measured eye lengths are not within the normal range, the retinal signal may occur in the high-frequency region of the image, where the depth-dependent signal drop limits the image quality.

Implementation of tunable optics in an OCT system also enables the extraction of ocular biometry parameters that demonstrate excellent correlation with a commercial optical biometer. The bias observed in axial length between the systems is most likely a result of the calibration procedure as well as the impact of correction of dispersion mismatch induced by eye structure. Better accuracy of the axial calibration might be obtained with the help of additional signal from a well-defined depth [18]. The higher intersession standard deviation measured for lens thickness, anterior chamber depth, and vitreous depth could be caused by a natural vibration of the crystalline lens position in the eye.

In conclusion, we developed a SS-OCT system integrated with tunable lens technology for comprehensive *in vivo* eye imaging. The tuning ability of the active element significantly improved the image quality of the ocular structures, also revealing details of microstructural changes in transparent media such as the

vitreous body. We recorded unprecedented (to our knowledge) 3D images of the vitreous that provided useful information such as opacifications in both vitreous attachment sites. Whole eye imaging, through quasi-simultaneous imaging of the anterior segment and the retina, has potential in ocular biometry applications. The approach with tunable lens technology presented in this report can be regarded as a versatile (volumetric) optical imaging platform with a number of *in vivo* ophthalmic applications.

REFERENCES

1. P. Artal, "Optics of the eye and its impact in vision: a tutorial," Adv. Opt. Photon. **6**, 340–367 (2014).
2. F. A. Midyett and S. K. Mukherji, *Orbital Imaging* (Elsevier, 2015).
3. A. Malhotra, F. J. Minja, A. Crum, and D. Burrowes, "Ocular anatomy and cross-sectional imaging of the eye," Semin. Ultrasound CT MRI **32**, 2–13 (2011).
4. L. Fanea and A. J. Fagan, "Review: magnetic resonance imaging techniques in ophthalmology," Mol. Vis. **18**, 2538–2560 (2012).
5. C. Enders, E.-M. Braig, K. Scherer, J. U. Werner, G. K. Lang, G. E. Lang, F. Pfeiffer, P. Noël, E. Rummeny, and J. Herzen, "Advanced non-destructive ocular visualization methods by improved X-ray imaging techniques," PLoS One **12**, e0170633 (2017).
6. I. Grulkowski, "Anterior segment OCT," in *Handbook of Visual Optics*, P. Artal, ed. (CRC Press, 2017), pp. 61–90.
7. I. Grulkowski, M. Gora, M. Szkulmowski, I. Gorczynska, D. Szlag, S. Marcos, A. Kowalczyk, and M. Wojtkowski, "Anterior segment imaging with spectral OCT system using a high-speed CMOS camera," Opt. Express **17**, 4842–4858 (2009).
8. C. Dai, C. Zhou, S. Fan, Z. Chen, X. Chai, Q. Ren, and S. Jiao, "Optical coherence tomography for whole eye segment imaging," Opt. Express **20**, 6109–6115 (2012).
9. S. H. Fan, L. Li, Q. Li, C. X. Dai, Q. S. Ren, S. L. Jiao, and C. Q. Zhou, "Dual band dual focus optical coherence tomography for imaging the whole eye segment," Biomed. Opt. Express **6**, 2481–2493 (2015).
10. X. Mao, J. T. Banta, B. Ke, H. Jiang, J. He, C. Liu, and J. Wang, "Wavefront derived refraction and full eye biometry in pseudophakic eyes," PLoS One **11**, e0152293 (2016).
11. M. Ruggeri, S. R. Uhlhorn, C. De Freitas, A. Ho, F. Manns, and J. M. Parel, "Imaging and full-length biometry of the eye during accommodation using spectral domain OCT with an optical switch," Biomed. Opt. Express **3**, 1506–1520 (2012).
12. J. G. Zhong, Y. L. Shao, A. Z. Tao, H. Jiang, C. Liu, H. C. Zhang, and J. H. Wang, "Axial biometry of the entire eye using ultra-long scan depth optical coherence tomography," Am. J. Ophthalmol. **157**, 412–420.e2 (2014).
13. H.-W. Jeong, S.-W. Lee, and B.-M. Kim, "Spectral-domain OCT with dual illumination and interlaced detection for simultaneous anterior segment and retina imaging," Opt. Express **20**, 19148–19159 (2012).
14. H. J. Kim, P. U. Kim, M. G. Hyeon, Y. Choi, J. Kim, and B. M. Kim, "High-resolution, dual-depth spectral-domain optical coherence tomography with interlaced detection for whole-eye imaging," Appl. Opt. **55**, 7212–7217 (2016).
15. I. Grulkowski, J. J. Liu, B. Potsaid, V. Jayaraman, C. D. Lu, J. Jiang, A. E. Cable, J. S. Duker, and J. G. Fujimoto, "Retinal, anterior segment and full eye imaging using ultrahigh speed swept source OCT with vertical-cavity surface emitting lasers," Biomed. Opt. Express **3**, 2733–2751 (2012).
16. A.-H. Dhalla, D. Nankivil, T. Bustamante, A. Kuo, and J. A. Izatt, "Simultaneous swept source optical coherence tomography of the anterior segment and retina using coherence revival," Opt. Lett. **37**, 1883–1885 (2012).
17. M. Gora, K. Karnowski, M. Szkulmowski, B. J. Kaluzny, R. Huber, A. Kowalczyk, and M. Wojtkowski, "Ultra high-speed swept source OCT imaging of the anterior segment of human eye at 200 kHz with adjustable imaging range," Opt. Express **17**, 14880–14894 (2009).
18. I. Grulkowski, J. J. Liu, J. Y. Zhang, B. Potsaid, V. Jayaraman, A. E. Cable, J. S. Duker, and J. G. Fujimoto, "Reproducibility of a long-range swept-source optical coherence tomography ocular biometry system and comparison with clinical biometers," Ophthalmology **120**, 2184–2190 (2013).
19. B. Kiss, O. Findl, R. Menapace, M. Wirtitsch, W. Drexler, C. K. Hitzenberger, and A. F. Fercher, "Biometry of cataractous eyes using partial coherence interferometry—clinical feasibility study of a commercial prototype I," J. Cataract Refract. Surg. **28**, 224–229 (2002).
20. J. Santodomingo-Rubido, E. A. H. Mallen, B. Gilmartin, and J. S. Wolffsohn, "A new non-contact optical device for ocular biometry," Br. J. Ophthalmol. **86**, 458–462 (2002).
21. P. J. Buckhurst, J. S. Wolffsohn, S. Shah, S. A. Naroo, L. N. Davies, and E. J. Berrow, "A new optical low coherence reflectometry device for ocular biometry in cataract patients," Br. J. Ophthalmol. **93**, 949–953 (2009).
22. K. Rohrer, B. E. Frueh, R. Wälti, I. A. Clemetson, C. Tappeiner, and D. Goldblum, "Comparison and evaluation of ocular biometry using a new noncontact optical low-coherence reflectometer," Ophthalmology **116**, 2087–2092 (2009).
23. L. P. J. Cruysberg, M. Doors, F. Verbakel, T. T. J. M. Berendschot, J. De Brabander, and R. M. M. A. Nuijts, "Evaluation of the Lenstar LS 900 non-contact biometer," Br. J. Ophthalmol. **94**, 106–110 (2010).
24. S. Srivannaboon, C. Chirapapaisan, P. Chonpimai, and S. Loket, "Clinical comparison of a new swept-source optical coherence tomography-based optical biometer and a time-domain optical coherence tomography-based optical biometer," J. Cataract Refract. Surg. **41**, 2224–2232 (2015).
25. A. Akman, L. Asena, and S. G. Güngör, "Evaluation and comparison of the new swept source OCT-based IOLMaster 700 with the IOLMaster 500," Br. J. Ophthalmol. **100**, 1201–1205 (2016).
26. K. Mishra, D. van den Ende, and F. Mugele, "Recent developments in optofluidic lens technology," Micromachines **7**, 102 (2016).
27. F. O. Fahrbach, F. F. Voigt, B. Schmid, F. Helmchen, and J. Huisken, "Rapid 3D light-sheet microscopy with a tunable lens," Opt. Express **21**, 21010–21026 (2013).
28. J. M. Jabbour, B. H. Malik, C. Olsovsky, R. Cuenca, S. Cheng, J. A. Jo, Y.-S. L. Cheng, J. M. Wright, and K. C. Maitland, "Optical axial scanning in confocal microscopy using an electrically tunable lens," Biomed. Opt. Express **5**, 645–652 (2014).
29. Y. Nakai, M. Ozeki, T. Hiraiwa, R. Tanimoto, A. Funahashi, N. Hiroi, A. Taniguchi, S. Nonaka, V. Boilot, R. Shrestha, J. Clark, N. Tamura, V. M. Draviam, and H. Oku, "High-speed microscopy with an electrically tunable lens to image the dynamics of in vivo molecular complexes," Rev. Sci. Instr. **86**, 013707 (2015).
30. I. Grulkowski, K. Szulzycki, and M. Wojtkowski, "Microscopic OCT imaging with focus extension by ultrahigh-speed acousto-optic tunable lens and stroboscopic illumination," Opt. Express **22**, 31746–31760 (2014).
31. J. P. Su, Y. Li, M. L. Tang, L. Liu, A. D. Pechauer, D. Huang, and G. J. Liu, "Imaging the anterior eye with dynamic-focus swept-source optical coherence tomography," J. Biomed. Opt. **20**, 126002 (2015).
32. M. Pircher, E. Götzinger, and C. K. Hitzenberger, "Dynamic focus in optical coherence tomography for retinal imaging," J. Biomed. Opt. **11**, 054013 (2006).
33. Y. K. K. Tao, S. K. Srivastava, and J. P. Ehlers, "Microscope-integrated intraoperative OCT with electrically tunable focus and heads-up display for imaging of ophthalmic surgical maneuvers," Biomed. Opt. Express **5**, 1877–1885 (2014).

34. Y.-H. Lin and H.-S. Chen, "Electrically tunable-focusing and polarizer-free liquid crystal lenses for ophthalmic applications," Opt. Express **21**, 9428–9436 (2013).

35. H. E. Milton, P. B. Morgan, J. H. Clamp, and H. F. Gleeson, "Electronic liquid crystal contact lenses for the correction of presbyopia," Opt. Express **22**, 8035–8040 (2014).

36. C. Dorronsoro, A. Radhakrishnan, J. R. Alonso-Sanz, D. Pascual, M. Velasco-Ocana, P. Perez-Merino, and S. Marcos, "Portable simultaneous vision device to simulate multifocal corrections," Optica **3**, 918–924 (2016).

37. I. Grulkowski, D. Jankowski, and P. Kwiek, "Acousto-optic interaction of a Gaussian laser beam with an ultrasonic wave of cylindrical symmetry," Appl. Opt. **46**, 5870–5876 (2007).

38. E. A. Villegas, E. Alcón, and P. Artal, "Optical quality of the eye in subjects with normal and excellent visual acuity," Invest. Ophthalmol. Vis. Sci. **49**, 4688–4696 (2008).

39. P. Pérez-Merino, S. Ortiz, N. Alejandre, A. de Castro, I. Jiménez-Alfaro, and S. Marcos, "Ocular and optical coherence tomography-based corneal aberrometry in keratoconic eyes treated by intracorneal ring segments," Am. J. Ophthalmol. **157**, 116–127.e1 (2014).